Communications in Nonlinear Science and Numerical Simulation 117 (2023) 106966

Contents lists available at ScienceDirect

Communications in Nonlinear Science and Numerical Simulation

journal homepage: www.elsevier.com/locate/cnsns

Research paper

Comparison between phase-field model and coarse-grained model for characterizing cell-resolved morphological and mechanical properties in a multicellular system

Guoye Guan [a,1], Xiangyu Kuang [a,1], Chao Tang [a,b,c,*], Lei Zhang [a,d,e,*]

[a] Center for Quantitative Biology, Peking University, Beijing 100871, China
[b] Peking-Tsinghua Center for Life Sciences, Peking University, Beijing 100871, China
[c] School of Physics, Peking University, Beijing 100871, China
[d] Beijing International Center for Mathematical Research, Peking University, Beijing 100871, China
[e] Center for Machine Learning Research, Peking University, Beijing 100871, China

ARTICLE INFO

Article history:
Available online 26 October 2022

Dataset link: https://doi.org/10.6084/m9.figshare.21070141

ABSTRACT

Embryonic development is a precise and complex process involving the cell morphology and mechanics interacting in space and time. The difficulty in quantitatively acquiring cellular morphological and mechanical information *in vivo* makes mathematical modeling a challenging problem and impedes model validation. Recently, the three-dimensional time-lapse live imaging and delineated developmental programs in the roundworm *Caenorhabditis elegans* provide an excellent platform for establishing quantitative models. In this paper, we study two popular computational models for multicellular systems, i.e., the phase-field model and the coarse-grained model, and compare their performance in characterizing the cell morphologies, cell adhesion, and cell stiffness in a real *C. elegans* embryo. We show that both models can capture cell–cell contact areas and heterogeneous cell adhesion, but only the phase-field model succeeds in inferring the heterogeneous cell stiffness by fitting cell shapes or cell–cell interface curvatures. Moreover, we demonstrate that the phase-field model converges to the coarse-grained model when increasing cell surface tension to dominance, obtaining a distance-dependent isotropic intercellular force.

1. Introduction

Cell morphology is generally defined as the three-dimensional (3D) distribution of a cell body, including multi-dimensional information such as the curvature and area of a cell–cell contact interface, cell shape, and its irregularity. It is a direct outcome of intracellular (e.g., cytoskeleton and growth) and extracellular (e.g., substrate and adhesion) forces [1–4]. The cellular mechanical properties, as well as the cell morphology, are tightly associated with cell fate no matter for a single cell or a cell cluster like the epidermis [5,6]. Exemplified by the cancerous cell in many circumstances, the smaller Young's modulus results in the high capability of deformation, migration, and invasion [7,8]. Unlike the cell morphology that can be acquired by *in vivo* imaging and automatic machine segmentation in a high-throughput way, the mechanical properties of a cell are much harder to measure without external disturbance to the system, in particular to the one

* Corresponding authors.
E-mail addresses: tangc@pku.edu.cn (C. Tang), zhangl@math.pku.edu.cn (L. Zhang).
[1] These authors contributed equally to this work.

https://doi.org/10.1016/j.cnsns.2022.106966
1007-5704/

with numerous proliferating, moving, deforming, and differentiating cells [9–14]. While direct measurement of cellular mechanical properties by advanced techniques like atomic force microscopy may affect the original biological activities due to external force [15–18], indirect inference by experimental observation and mechanical model or its derived features is an emerging strategy nowadays [19–21]. For example, Petridou et al. estimated the dynamic change of cell adhesion in zebrafish blastoderm by analyzing the two-dimensional (2D) contact angle among neighbor cells and environmental fluid, revealing a down-to-up manner in cell adhesion at a population level [21]. Nonetheless, it is elusive if such inference can reach the cellular level where the adhesion, as well as other mechanical properties, might be distributed unevenly. Thus, model selection and performance evaluation become practical problems.

Comparison of mathematical models for simulating biological scenes has been a long-term focus in applied mathematics and computational biology [22–24]. Especially, it was previously proved that the simulations of cellular or multicellular morphology by different mechanical models have distinguishable outputs [24]. Apart from the discrepancy between models, quantitative estimation of the difference between simulation and experiment are largely in lack. From the experimental perspective, the difficulty in acquiring cellular morphological and mechanical information *in vivo* hampers the model validation.

Remarkably, the advance in 3D time-lapse live imaging on *C. elegans* embryonic development provided an excellent platform to check the validity of mechanical models [11,25,26]. Besides, the *C. elegans* embryo is an advantageous material because its cell fate, cell position, cell division timing, and cellular mechanical properties are highly unique for each cell, enabling us to check the model down to single-cell resolution [1,27–29]. The first mechanical model for *C. elegans* embryonic development used a number of interacting particles to simulate the shape of a cell, and successfully generated the cell-arrangement patterns and cell shapes that resemble the true ones up to 4-cell stage [30,31]. However, this model contains many biologically-relevant parameters which are hard to measure; therefore, its development and application are somewhat stuck in this field. Later, some researchers applied a coarse-grained model where a cell is simplified into only one single point, and the intercellular forces are distance-dependent. Unlike the former one, the coarse-grained model has very few parameters but still shows good performance in recapitulating the stereotypic cell-arrangement patterns observed in a real embryo [20,32–35]. Recently, the phase-field model, which describes a cell with a diffusive scalar field, has been proposed to study *C. elegans* embryonic morphogenesis effectively [4,36,37]. Both the phase-field model and coarse-grained model have been developed using the *in vivo* data of *C. elegans* embryonic development. Even so, these two popular models have never been compared parallelly to test their performance in characterizing the cell-resolved morphological and mechanical properties in reality.

In this paper, we perform comprehensive comparisons of the phase-field model and coarse-grained model in characterizing the cell morphologies, cell adhesion, and cell stiffness by using the cell morphologies in 2- and 4-cell *C. elegans* embryos as a reference, which have been documented publicly [11]. The computational results show that both models can capture the cell morphologies and infer the heterogeneous cell adhesion by fitting the cell–cell contact areas, but only the phase-field model succeeds in inferring the heterogeneous cell stiffness by fitting the cell shapes. Finally, we analyze the performance and limit of both models and explore in what conditions they will converge together.

2. Model establishment

In recent years, the phase-field model and coarse-grained model are continuously optimized with experimental data and used for simulating and studying *C. elegans* embryonic cell-arrangement patterns with excellent performance (Fig. 1) [4,20,32–39]. Here, we establish the frameworks of these two models for their comprehensive comparisons.

2.1. Formulation of the phase-field model

The phase-field model is a diffuse interface method and has been proved to be capable of reconstructing the *C. elegans* embryonic morphologies [4,36–38]. In this model, a cell is represented by a scalar order parameter $\phi_i(\boldsymbol{r})$ that ranges from 0 (outside of the cell) to 1 (inside of the cell), where i is the cell identity and $\boldsymbol{r} \in \boldsymbol{R}^3$ is the 3D space variable. The cell is governed by volume constriction, surface tension, repulsion from the eggshell, and repulsion and attraction from the neighbor cells [4,38]. The eggshell is idealized as an ellipsoid in which the three axes are parallel to the x (anterior–posterior, A–P), y (left–right, L–R), and z (dorsal–ventral, D–V) axes of the rectangular coordinate system, respectively; the regions $|y| > w_{\max}$ are cut off to resemble the artificial lateral compression during *in vivo* imaging [11].

The phase-field function of the eggshell is given by:

$$\phi_e = \frac{1 + \tanh \frac{d(x,y,z)}{\sqrt{2}\epsilon}}{2}, \tag{1}$$

where $\epsilon = \frac{\sqrt{2}}{20}$ controls the boundary width of the eggshell; $d(x, y, z)$ is the distance of a point (x, y, z) in space to the eggshell and reads:

$$d(x,y,z) = \min\left\{ \sqrt{x^2 + \frac{L_{x/\mathrm{A-P}}^2}{L_{y/\mathrm{L-R}}^2} y^2 + \frac{L_{x/\mathrm{A-P}}^2}{L_{z/\mathrm{D-V}}^2} z^2} - L_{\mathrm{A-P}},\ |y| - w_{\max} \right\}, \tag{2}$$

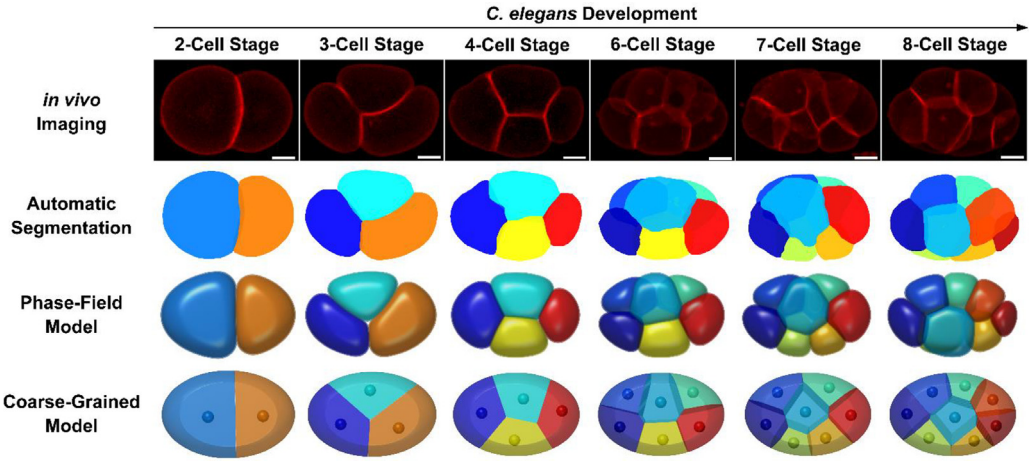

Fig. 1. Typical embryonic morphologies during 2- to 8-cell *C. elegans* development. Regarding the *in vivo* imaging (1st row) and automatic segmentation (2nd row), the 2- to 4-cell morphologies are obtained from [4] and the 6- to 8-cell morphologies are obtained from [11]; a scalar bar of 10 μm is plotted at the bottom right of each *in vivo* image; the automatic segmentation is executed with CShaper [11]. The 3rd and 4th rows show the *in silico* embryonic morphologies reconstructed by the phase-field model and coarse-grained model respectively.

where $L_{x/\mathrm{A-P}} = 27.7846\ \mu\mathrm{m}$, $L_{y/\mathrm{L-R}} = 14.7022\ \mu\mathrm{m}$, $L_{z/\mathrm{D-V}} = 18.3778\ \mu\mathrm{m}$ are the lengths of the ellipsoid's semimajor axes and $w_{\max} = 10.1188\ \mu\mathrm{m}$; the value assignments above are obtained from experimental data (the details of the eggshell setting are given in Appendix A). Note that $\phi_{\mathrm{e}} = 1$ and $\phi_{\mathrm{e}} = 0$ represent the outside and inside of the eggshell respectively.

Two fundamental equations lay a foundation for the phase-field model that consists of N cells in the space Ω:

A. The cell volume is controlled to be constant over time by limiting the relative error between simulated and experimental volumes:

$$\boldsymbol{F}_{\mathrm{volume}} = M\left[\frac{\int_{\Omega}\phi_i \mathrm{d}\boldsymbol{r}}{V_i(t)} - 1\right]\boldsymbol{n}, \tag{3}$$

where $M = 8$ denotes the strength of the volume constriction; $V_i(t)$ is the designated volume at time point t; $\boldsymbol{n}$ is the unit vector perpendicular to the cell boundary and pointing inward the cell.

B. A repulsive force is imposed between cells and between cells and the eggshell, to prevent the overlap among different phase fields:

$$\boldsymbol{F}_{\mathrm{repulsion}} = \left(g\phi_i\sum_{j\neq i}^{N}\phi_j^2 + g_{\mathrm{e}}\phi_i\phi_{\mathrm{e}}^2\right)\frac{\nabla\phi_i}{|\nabla\phi_i|^2}, \tag{4}$$

where $g = 1.6$ and $g_{\mathrm{e}} = 16$ denotes the strength of the repulsive force between cells and between cells and the eggshell, respectively. With these forces, the phase fields of the cells and the eggshell are excluded from each other. Furthermore, another two key mechanical forces are introduced to formulate the cellular and multicellular mechanics:

C. Cell adhesion is described by the attractive force between two cells:

$$\boldsymbol{F}_{\mathrm{adhesion}} = \sum_{j\neq i}^{N}\sigma_{i,j}\nabla\phi_j, \tag{5}$$

where $\sigma_{i,j}$ is non-negative and denotes the adhesion strength between cell i and cell j; ∇ is the gradient operator.

D. Cell stiffness is represented by the cell surface tension that drives a cell to be spherical with less surface area as well as less deformation:

$$\boldsymbol{F}_{\mathrm{tension}} = -\gamma_i\left[\Delta\phi_i - cW'(\phi_i)\right]\frac{\nabla\phi_i}{|\nabla\phi_i|^2}, \tag{6}$$

where γ_i is positive and denotes the stiffness or surface tension of cell i; $c = 1$ controls the boundary width of the cell; $W(\phi_i)$ is a double-well function that binarizes ϕ_i into 0 and 1 ($W(\phi_i) = \phi_i^2(\phi_i - 1)^2$ and $W'(\phi_i) = 2\phi_i(\phi_i - 1)(2\phi_i - 1)$); Δ is the Laplacian operator. Here, we consider all cells as intrinsically isotropic and their natural shape without any external force imposed is spherical; this morphological and mechanical character is

attributed to the actin filaments (i.e., F-actin) in reality, which generate the tensile force in the cell cortex and minimize the surface area of the cell membrane and has been recognized as a key contributor to cell stiffness [8]. The effect of cell surface tension γ in generating the resistance against external force and consequent deformation is equivalent to that of cell stiffness [38]; thereof, in this paper, we use cell surface tension to represent cell stiffness and omit the other factors involved in cell stiffness like nuclear stiffness [40,41].

Then the system evolves in an overdamped environment as follows:

$$\frac{\partial \phi_i}{\partial t} = -\frac{1}{\tau}\left(\boldsymbol{F}_{\text{volume}} + \boldsymbol{F}_{\text{repulsion}} + \boldsymbol{F}_{\text{adhesion}} + \boldsymbol{F}_{\text{tension}}\right) \cdot \nabla \phi_i, \tag{7}$$

where $\tau = 2.62$ denotes the environmental viscosity [42].

The cell boundary in the phase-field model is described as the diffusive interface where $\phi_i(\boldsymbol{r})$ transits from 1 to 0. Thus, the membrane area of cell i can be approximated by the area of the isosurface Γ_i that defines the cell boundary:

$$A_i = \int_{\Gamma_i} \mathrm{d}s, \tag{8}$$

where $\Gamma_i = \left\{\boldsymbol{r} \in \boldsymbol{R}^3 \middle| \phi_i(\boldsymbol{r}) \equiv 0.34\right\}$ and $\mathrm{d}s$ is the area of its surface element. For the contact interface between cell i and cell j, the corresponding area $A_{i,j}$ is calculated by:

$$A_{i,j} = \frac{\int_{\Gamma_{i,j}} \mathrm{d}s + \int_{\Gamma_{j,i}} \mathrm{d}s}{2}. \tag{9}$$

where $\Gamma_{i,j} = \{\boldsymbol{r} \in \Gamma_i | \phi_j(\boldsymbol{r}) \geq 0.2\}$ is a subset of Γ_i and is located in the boundary of cell j.

In this paper, we set the three-dimensional grid size for phase-field simulation as 120×60×80 in the x, y, and z directions, and the pixel resolution is 0.5 μm/pixel. These settings have been proved to be accurate enough to generate the 1- to 8-cell *C. elegans* embryonic morphologies with experimentally-observed mechanical parameters [38]. Then the eggshell and embryo are placed in the center of the grid. All the value assignments for the parameters in the phase-field model and the reasons for taking the values are summarized in Table S1. The iteration of the phase fields per time step is executed using a second-order semi-implicit scheme coupled with a stabilization term, as described in [38]. Throughout all phase-field simulations in this paper, the time step is set as 0.2 unless otherwise specified, and the simulation ends when the root-mean-square velocity of all cell centers is beneath 1×10^{-4}.

2.2. Formulation of the coarse-grained model

The coarse-grained model has been developed to study *C. elegans* embryonic development for a decade [20,32–35,39]. The model simplifies a cell into a single point which is quantitatively described with only its three spatial coordinates. Cellular interaction is repulsive and attractive corresponding to the short and long distances between cells respectively; if the distance between a cell and eggshell is shorter than the cell radius, the cell is subject to an additional repulsion orienting inward the embryo. The forces above are formulated as [34]:

$$\boldsymbol{F}_{i,j} = \gamma'_{i,j}\boldsymbol{e}_{i,j} \cdot \begin{cases} \dfrac{-\left[d_{i,j} - \frac{1}{\sigma_{i,j}}\left(R_i + R_j\right)\right]}{\frac{1}{\sigma_{i,j}}\left(R_i + R_j\right)} & 0 < d_{i,j} \leq \dfrac{\left(1 + \frac{1}{\sigma_{i,j}}\right)\left(R_i + R_j\right)}{2} \\ \dfrac{\left[d_{i,j} - \left(R_i + R_j\right)\right]}{\frac{1}{\sigma_{i,j}}\left(R_i + R_j\right)} & \dfrac{\left(1 + \frac{1}{\sigma_{i,j}}\right)\left(R_i + R_j\right)}{2} < d_{i,j} \leq R_i + R_j \\ 0 & R_i + R_j < d_{i,j} \end{cases}, \tag{10}$$

$$\boldsymbol{F}_{i,\mathrm{e}} = \gamma_{\mathrm{e}}\boldsymbol{e}_{i,\mathrm{e}} \cdot \begin{cases} R_i - d_{i,\mathrm{e}} & 0 < d_{i,\mathrm{e}} < R_i \\ 0 & R_i < d_{i,\mathrm{e}} \end{cases}, \tag{11}$$

where R_i and R_j denote the equivalent radius of cell i and cell j, calculated with the cell volume V_i and V_j measured *in vivo*, namely, $R_i = \sqrt[3]{\frac{3V_i}{4\pi}}$ and $R_j = \sqrt[3]{\frac{3V_j}{4\pi}}$; $\boldsymbol{F}_{i,j}$ and $\boldsymbol{F}_{i,\mathrm{e}}$ denote the force imposed on cell i from cell j and eggshell; $d_{i,j}$ and $d_{i,\mathrm{e}}$ denote the distance from cell i to cell j and eggshell; $\boldsymbol{e}_{i,j}$ and $\boldsymbol{e}_{i,\mathrm{e}}$ denotes the unit vector pointing from cell j and eggshell (contact point) to cell i; regarding the contact point, the distance between cell i to all the points of eggshell is calculated, then the contact point is determined if the shortest distance is smaller than the cell radius and the corresponding point is where the contact is established; γ_{e} denotes the stiffness of eggshell; as the force between cells is pairwise, $\gamma'_{i,j}$ represents the joint effect of the stiffness of two cells, unlike the γ_i in the phase-field model (Eq. (6)) which represents the stiffness of one specific cell. $\sigma_{i,j}$ still denotes the adhesion strength between cell i and cell j but is no smaller than 1; $\frac{1}{\sigma_{i,j}}\left(R_i + R_j\right)$ is the balance distance between cell i and cell j where the interacting force is zero.

Then the system evolves in an overdamped environment as follows:

$$\frac{\mathrm{d}\boldsymbol{r}_i}{\mathrm{d}t} = \frac{1}{\tau}\left(\sum_{j \neq i}^{N} \boldsymbol{F}_{i,j} + \boldsymbol{F}_{i,\mathrm{e}}\right). \tag{12}$$

The description of cell–cell and cell–eggshell forces by piecewise linear functions (Eqs. (10) and (11)) and the assumed overdamped condition (Eq. (12)) have been reported to be able to well reproduce the *C. elegans* cell-arrangement patterns in reality (Fig. 1) [20,32–35], but its applicability in capturing *in vivo* cell morphologies and inferring cellular mechanical properties is largely unknown.

Here, we set $\gamma_e = 1$ to serve as the mechanical unit and $\tau = 1$ to serve as the time unit, then the coarse-grained system is governed by only two variables: γ' and σ. By fitting the coarse-grained model onto the experimental cell-arrangement patterns at 4-, 8-, 12-, and 26-cell stages during *C. elegans* embryonic development, we obtain the homogeneous central parameters $\gamma' = 0.04, \sigma = \frac{1}{0.85} \approx 1.18$ (Appendix B). All the value assignments for the parameters in the coarse-grained model and the reasons for taking the values are summarized in Table S1. Two requirements are necessary for filtering the outputs of subsequent simulations: 1. the deviation between simulated and experimental cell positions must be smaller than the equivalent cell radius, guaranteeing the correctness of cell arrangement; 2. The cell–cell contact relationship must be correct. Using the cell positions as centers, the cell–cell contact area and cell shape are generated by Voronoi tessellation [43–46].

3. Ground truth for *C. elegans* embryonic development

3.1. Cell morphologies

In a previous work [11], a total of 17 *C. elegans* embryos (labeled as Sample 04 to Sample 20 in the original literature) were imaged no later than 4-cell stage at an interval of 1.39 min. The cell membrane was tagged with mCherry (red fluorescent protein) and is subject to automatic machine segmentation, producing statistical information on cell morphology like cell–cell contact area and cell shape (Fig. 2(A) and (B)). Here, we primarily focus on the final cell morphologies at 4-cell stage (cell names: ABa, ABp, EMS, and P2) and use the 17 embryos to calculate the statistical shape distribution for each cell, showing that the cell shapes are highly conserved with slight variation (Fig. 2(C)). The reference is placed in a $120 \times 60 \times 80$ rectangular mesh with a spatial resolution of 0.5 μm/pixel, consistent with the one used in the phase-field simulation. Then the distributions are merged and binarized into an average embryo, by comparing the existence probability of each cell for each pixel (Fig. 2(D)). It should be pointed out that, the final cell morphologies at 2-cell stage (cell names: AB and P1) will be explored independently later as it is only covered by two embryos (Sample 07 and Sample 15); the 3-cell stage is completely skipped for that its duration is as small as around 2 min, near the temporal resolution of this dataset [47,48]. The experimentally recorded 2- to 4-cell *C. elegans* morphodynamics in Sample 07 and Sample 15 are shown in Movies S1–S2.

Experimental measurements show that the volumes of any specific cell at the last moment of 2- and 4-cell stages are nearly constant among embryos, with a coefficient variation (standard deviation over average) always smaller than 0.07 (Table S2). Besides, a cell's volume is also nearly constant during its lifespan, with a coefficient variation always smaller than 0.02 (Table S3). Thus, for the 4-cell stage, we neglect the slight difference in cell volume among embryos and use the experimentally-measured average values for simulation; for either cell at the 2-cell stage, the volume is assigned with the sum of its two daughter cells' average volumes, considering the larger sample size and the volume constancy of embryo over time.

3.2. Cell adhesion and cell stiffness

The ground truth for the heterogeneous distribution of cell adhesion and cell stiffness is acquired according to previous experimental reports.

A. At 4-cell stage, the accumulation of adhesive protein (Epithelial cadherin, i.e., E-cadherin) in EMS-P2 contact is lower than the ones in other contacts [20,29]. Such heterogeneity has been demonstrated by both fluorescence imaging and evaluation of cell–cell distance.
B. A very recent experimental study discovered that the cell stiffness during ascidian embryonic development oscillates like a wave over time: the cell becomes stiffer when dividing and softer in the middle of its lifespan [49]. The phenomenon is attributed to the reorganization of F-actin in the cell cortex and was demonstrated by measuring the cell stiffness with atomic force microscopy. According to this rule, the unsynchronized cell division timings in *C. elegans* embryo confer heterogeneous cell stiffness: ABa = ABp > EMS > P2 at the last moment of 4-cell stage and AB > P1 at the last moment of 2-cell stage (Fig. 3) [28,47,48].

3.3. Evaluation of variation between simulation and experiment

We utilize the experimentally-measured cell–cell contact area and cell shape to fit the parameters of cell adhesion ($\sigma_{i,j}$) and cell stiffness (γ_i or $\gamma'_{i,j}$), respectively. In theory, one can obtain the proper values by minimizing the variation

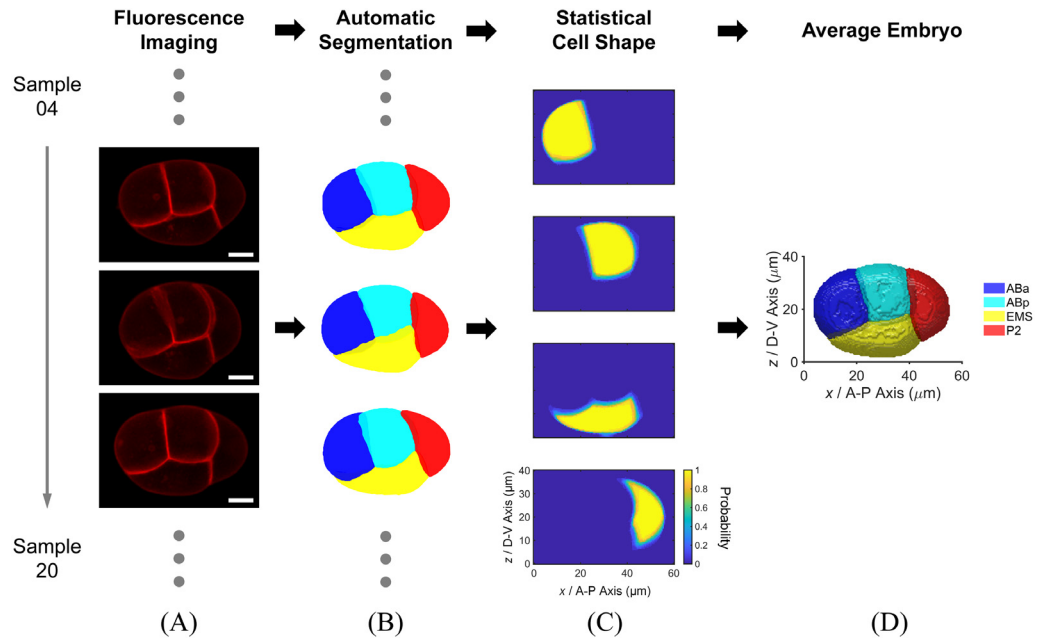

Fig. 2. The pipeline for collecting cell morphologies, including (A) fluorescence imaging, (B) automatic segmentation, (C) calculating statistical cell shape, and (D) establishing an average embryo. The fluorescence images at the last time point of 4-cell stage are shown in (A), with a scale bar representing 10 μm in reality; their segmented results are shown in (B); the data of both (A) and (B) are acquired from a previous dataset [11].

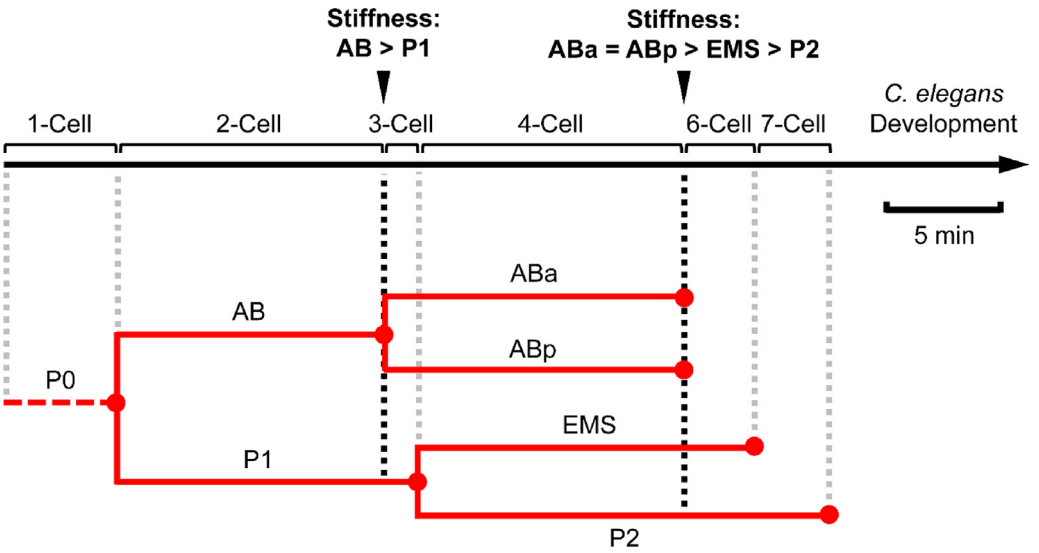

Fig. 3. The cell division timing of ABa, ABp, EMS, P2, and their ancestors. The data is obtained from a previous dataset [28].

between simulation and experiment, and those values obtained should match the ground truth if the model is accurate enough. Here, the variation of contact area between cell i and cell j is defined by:

$$\eta_{i,j} = \left| \frac{a_{i,j} - A_{i,j}}{a_{i,j}} \right|, \tag{13}$$

where $a_{i,j}$ denotes the experimental contact area between cell i and cell j. On the other hand, the variation of cell shape is defined as the difference of pixels between the simulated and experimental cellular regions:

$$\eta_i = \frac{\delta p_i + \delta P_i}{2p_i}. \tag{14}$$

where p_i denotes the pixel number of cell i in the experimental average embryo (Fig. 2(D)); δp_i is the number of the pixels that belong to the experimental but not the simulated shape; δP_i is the number of the pixels that belong to the simulated but not the experimental shape; if there is no overlap between simulated and experimental cellular regions, $\eta_i = 1$. Below, we used the mean variations of all cell–cell contacts ($\overline{\eta}_{\text{contact}}$) or all cell shapes ($\overline{\eta}_{\text{shape}}$) to judge how well the simulation fits the experiment.

4. Comparison between the phase-field model and coarse-grained model

Below, we will systematically scan the parameters of cell adhesion and cell stiffness and generate the cell morphologies with the phase-field model and coarse-grained model, figuring out if those models can characterize the multicellular morphological and mechanical properties at single-cell resolution.

4.1. Fitting the parameter of cell adhesion with the cell–cell contact area

Regarding the 4-cell stage of *C. elegans* development, our previous works on the phase-field model demonstrated that the assignments of weak adhesion (σ_{W}) on EMS-P2 contact and strong adhesion (σ_{S}) on other contacts provide the smallest mean variation of cell–cell contact areas between *in vivo* and *in silico* [4,38]. Nevertheless, it is still unknown if the low-dimensional coarse-grained model can also reconstitute this asymmetric cell adhesion distribution by fitting the cell–cell contact areas. Thus, we scan the σ_{W} (specified for EMS-P2 contact) and σ_{S} (specified for ABa-ABp, ABa-EMS, ABp-EMS, and ABp-P2 contacts) in both the phase-field model and the coarse-grained model. The volumes of the 4 cells (i.e., ABa, ABp, EMS, and P2) are inputted with the values measured experimentally (Fig. 2(B), Table S2) [11]; the cell stiffness is set as constant for all cells in both models ($\gamma_i \equiv 0.25$ and $\gamma'_{i,j} \equiv 0.04$) (Table S1). It turns out that the minimal $\overline{\eta}_{\text{contact}}$ is achieved when $\sigma_{\text{EMS,P2}} = \sigma_{\text{W}} < \sigma_{\text{S}}$ for not only the phase-field model but also the coarse-grained model (Fig. 4(A)–(C),Movies S3–S4).

To exclude the possibility that the success of the coarse-grained model is a coincidence relying on Voronoi tessellation, we further test another method for identifying the cell–cell contact interface and calculating its area: the cells are approximated as perfect spheres where the areas of their cross-sections are examined; to ensure the proper establishment of the cross-section between cell i and cell j, we demand that the three lengths $R_i, R_j, d_{i,j}$ form an acute triangle. This quantitative method also outputs the optimal parameter combination $\sigma_{\text{EMS,P2}} = \sigma_{\text{W}} = 1.25 < 1.74 = \sigma_{\text{S}}$ by minimizing $\overline{\eta}_{\text{contact}}$ (Fig. 5(A) and (B), Movie S5), further supporting the ability of the coarse-grained model in capturing heterogeneous cell adhesion. This result is in accordance with a previous study, in which the addition of asymmetric cell adhesion ($\sigma_{\text{ABa,ABp}} = \sigma_{\text{ABa,EMS}} = \sigma_{\text{ABp,EMS}} = \sigma_{\text{ABp,P2}} > \sigma_{\text{EMS,P2}}$) in the coarse-grained model is essential for reproducing the cell-arrangement patterns found in real embryos [20]. Even though the cell is simplified into a single point, the cell–cell distance is still monotonically decreasing with both cell adhesion and cell–cell contact area, thus the coarse-grained model is sufficient for characterizing those features.

4.2. Fitting the parameter of cell stiffness with the cell shape

Although amplification of γ_i and $\gamma'_{i,j}$ can lengthen the distance between neighbor cells in both the phase-field model and coarse-grained model, resembling the effect of cell stiffness, it is still unclear if the morphological output (e.g., cell shape) matches the reality [38]. We first examine if the cell stiffness relationship $\gamma_{\text{ABa}} = \gamma_{\text{ABp}} > \gamma_{\text{EMS}} > \gamma_{\text{P2}}$ at 4-cell stage can be inferred directly by the phase-field model (Fig. 3). In the first round of parameter scanning, we assume that the two pairs of sister cells have differential cell stiffness, namely, $\gamma_{\text{ABa}} = \gamma_{\text{ABp}} = \gamma_{\text{ABa/ABp}} \neq \gamma_{\text{EMS/P2}} = \gamma_{\text{EMS}} = \gamma_{\text{P2}}$. After the biocomponent scanning on $\gamma_{\text{ABa/ABp}}$ and $\gamma_{\text{EMS/P2}}$ from 0.2 to 6.0 in a step of 0.1, the mean variation of cell shapes ($\overline{\eta}_{\text{shape}}$) is minimized when ABa and ABp are harder than EMS and P2 ($\gamma_{\text{ABa/ABp}} = 1.6$, $\gamma_{\text{EMS/P2}} = 0.2$) (Fig. 6(A) and (B), Movie S6). We further separate $\gamma_{\text{EMS/P2}}$ into γ_{EMS} and γ_{P2} from $\gamma_{\text{EMS/P2}}$ and vary them from 0.1 to 1.5 in a step of 0.05. The global minimum of $\overline{\eta}_{\text{shape}}$ is achieved when $\gamma_{\text{EMS}} = 0.25$, $\gamma_{\text{P2}} = 0.15$, suggesting that P2 should be slightly softer than EMS (Fig. 6(A) and (B), Movie S7). The cell stiffness relationship is fairly reproduced, demonstrating the power of the phase-field model for simulating cell stiffness and cell shape.

Regarding the coarse-grained model, the binary cell stiffness relationship ABa = ABp > EMS = P2 is equivalent to the ternary value assignments on γ': $\gamma'_{\text{ABa,ABp}} = \gamma'_{\text{S}} > \gamma'_{\text{ABa,EMS}} = \gamma'_{\text{ABp,EMS}} = \gamma'_{\text{ABp,P2}} = \gamma'_{\text{M}} > \gamma'_{\text{EMS,P2}} = \gamma'_{\text{W}}$. We enumerate the three values from 0.01 to 0.1 in a step of 0.01 (the upper limit is one order of magnitude smaller than the eggshell stiffness $\gamma_{\text{e}} = 1$). Using the Voronoi tessellation to construct cell shapes, the minimization of $\overline{\eta}_{\text{shape}}$ cannot locate the values that obey $\gamma'_{\text{S}} > \gamma'_{\text{M}} > \gamma'_{\text{W}}$, so the coarse-grained model fails to recapitulate the cell stiffness by fitting cell shapes (Fig. 6 (A) and (C)).

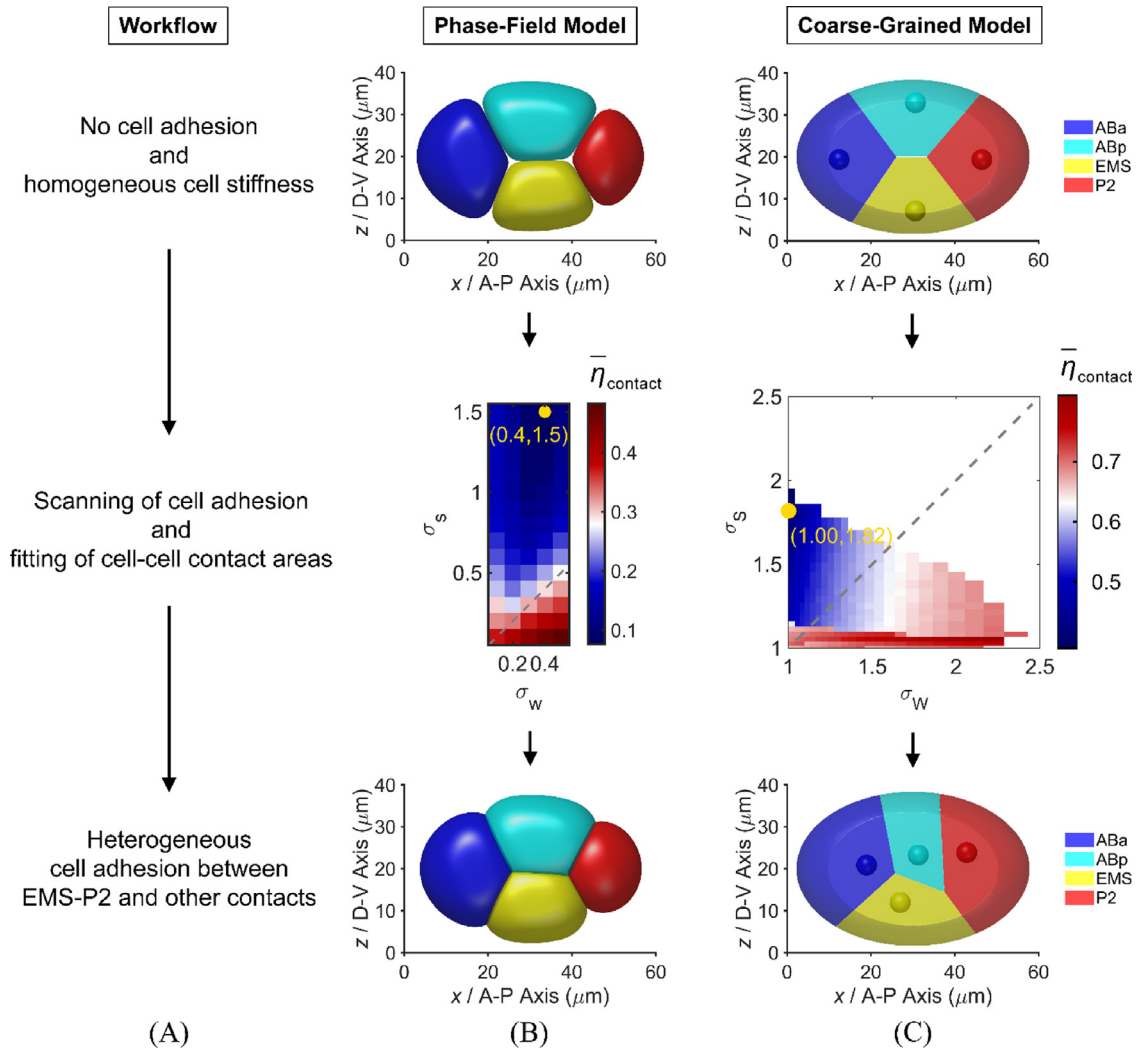

Fig. 4. The fitting of cell–cell contact areas at 4-cell stage by scanning cell adhesion. (A) Computational workflow for inferring heterogeneous cell adhesion. (B) Results of the phase-field model. (C) Results of the coarse-grained model. The outputted $\overline{\eta}_{\text{contact}}$ are illustrated by heatmaps, with the gray dashed lines labeling the homogeneous values and the yellow points labeling the optimal values.

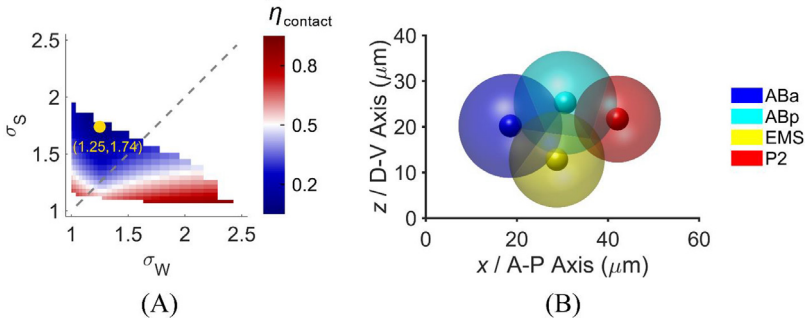

Fig. 5. The fitting of cell–cell contact areas at 4-cell stage by scanning cell adhesion in the coarse-grained model, where the cells are approximated as perfect spheres and their cross-sections are used for calculating contact areas. (A) The outputted $\overline{\eta}_{\text{contact}}$ are illustrated by heatmaps, with the gray dashed lines labeling the homogeneous values and the yellow points labeling the optimal values. (B) The optimal embryonic morphology.

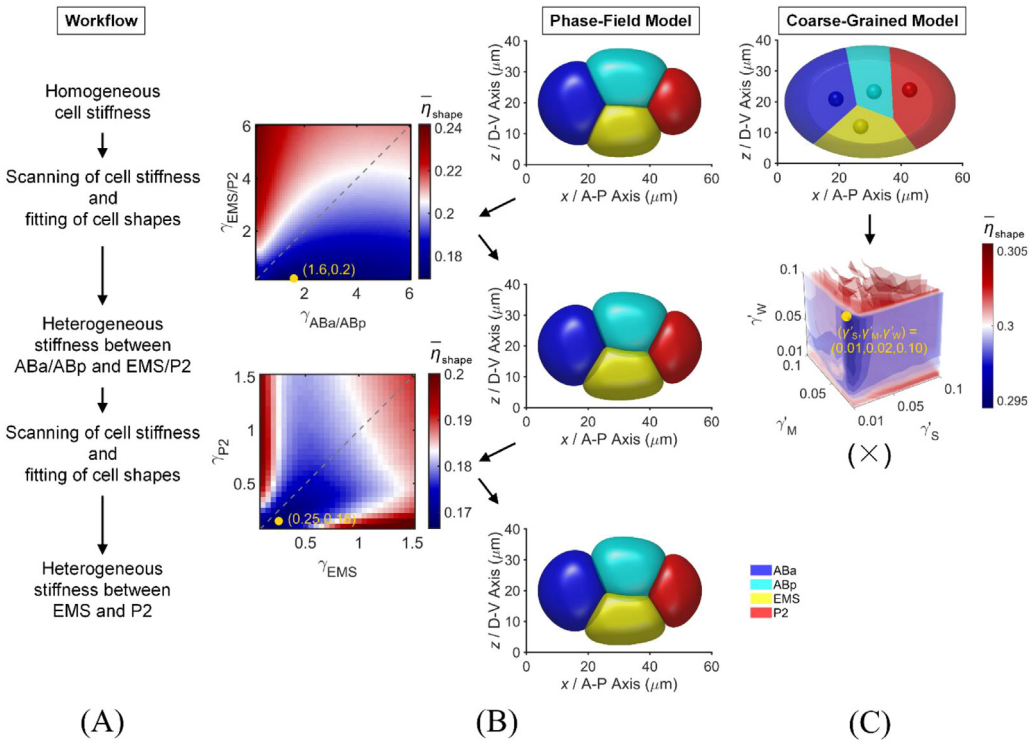

Fig. 6. The fitting of cell shapes at 4-cell stage by scanning cell stiffness. (A) Computational workflow for inferring heterogeneous cell stiffness. (B) Results of the phase-field model. (C) Results of the coarse-grained model; "×" means that the inference of heterogeneous cell stiffness fails. The outputted $\overline{\eta}_{\text{shape}}$ are illustrated by heatmaps, with the gray dashed lines labeling the homogeneous values and the yellow points labeling the optimal values.

4.3. Advantages of the phase-field model compared to the coarse-grained model

To elucidate why the phase-field model outperforms the coarse-grained model when simulating cell stiffness and cell shape, we choose a simpler situation, the last moment of 2-cell stage, where the contact interface is protruding from AB to P1 due to higher cell surface tension as shown in Fig. 7(A) and (D) [1,30]. Using the two embryos (Sample 07 and Sample 15) imaged from 2-cell stage, we apply the phase-field model without cell adhesion considered (i.e., $\sigma_{\text{AB,P1}} = 0$) and scan both γ_{AB} and γ_{P1} in the range from 0.1 to 3 in a step of 0.1. It is shown that the stiffness heterogeneity can be easily inferred by minimizing $\overline{\eta}_{\text{shape}}$, along with a curved contact interface orientating correctly (Fig. 7(B) and (E)). On the other hand, the repulsion between two neighbor cells is governed by only one spring-like parameter ($\gamma'_{\text{AB,P1}}$) in the coarse-grained model, so the heterogenous stiffness between AB and P1 is impossible to be derived (Fig. 7(C) and (F)). Moreover, the cell shape produced by Voronoi tessellation is always convex polyhedron so it cannot capture the interface curvature as the phase-field model does.

The information on cell–cell interface curvature is also incorporated into the cell shape fitting at 4-cell stage (Fig. 6(A) and (B)). Planar fitting on the five cell–cell contact interfaces shows that the coefficient of determination R^2 in ABa-ABp contact is over 0.55 while all the others are smaller than 0.14, corresponding to the similar or same stiffness in ABa and ABp due to their synchronous lifespans (Figs. 3 and 8(A)) [28,49]. Next, we calculate the curvature radius of all the remaining interfaces by fitting them with a sphere. The interface orientations defined by the fitted spheres obey the ground-truth relationship ABa = ABp > EMS > P2 that can be derived with cell shape optimization in Fig. 6(A), as all the stiffer cell protrudes toward the softer one (Fig. 8(A)–(E)). This morphological analysis indicates that the construction of a curved cell boundary in a model is crucial for delineating cell stiffness and cell shape, explaining the outperformance of the phase-field model in this problem. It is worth pointing out that, varying the stiffness and volume of AB and P1 at 2-cell stage reveals that with the same stiffness level, the larger cell protrudes toward the smaller one (Fig. S1 (A)); in other words, a large cell volume can compensate for a small cell stiffness regarding the cell–cell interface curvature (Fig. S1 (B)). Thus, the cell stiffness heterogeneity should not be inferred solely by the cell–cell interface curvature obtained in experiment, and the phase-field model is necessarily needed for considering the effect of other morphological and mechanical properties.

The importance of cell–cell interface curvature can be illustrated clearly by gradually strengthening the cell stiffness in the phase-field model, which makes the cells rounder and rounder. We quantify such effect using the cell shape

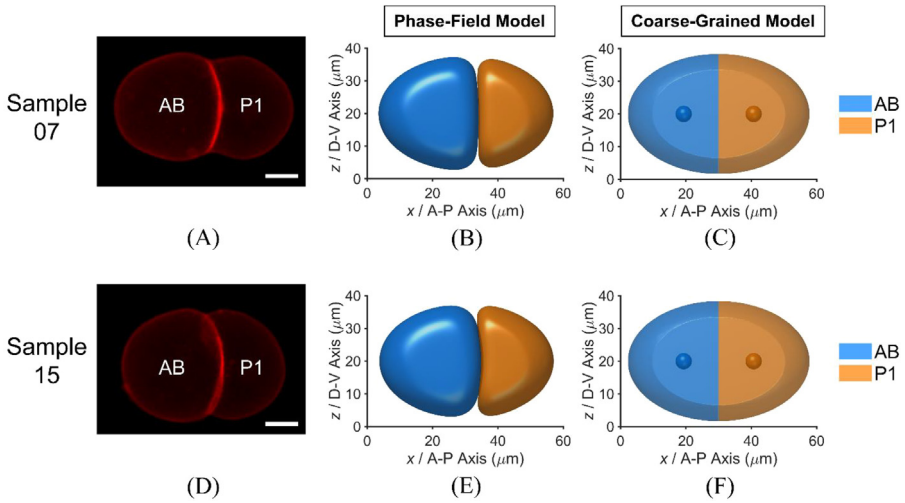

Fig. 7. The fitting of cell shapes at 2-cell stage by scanning cell stiffness. (A, D) Experimental morphologies with a scale bar representing 10 μm in reality. (B, E) The optimal embryonic morphologies of the phase-field model. (C, F) The optimal embryonic morphologies of the coarse-grained model. Cell adhesion is ignored in all simulations.

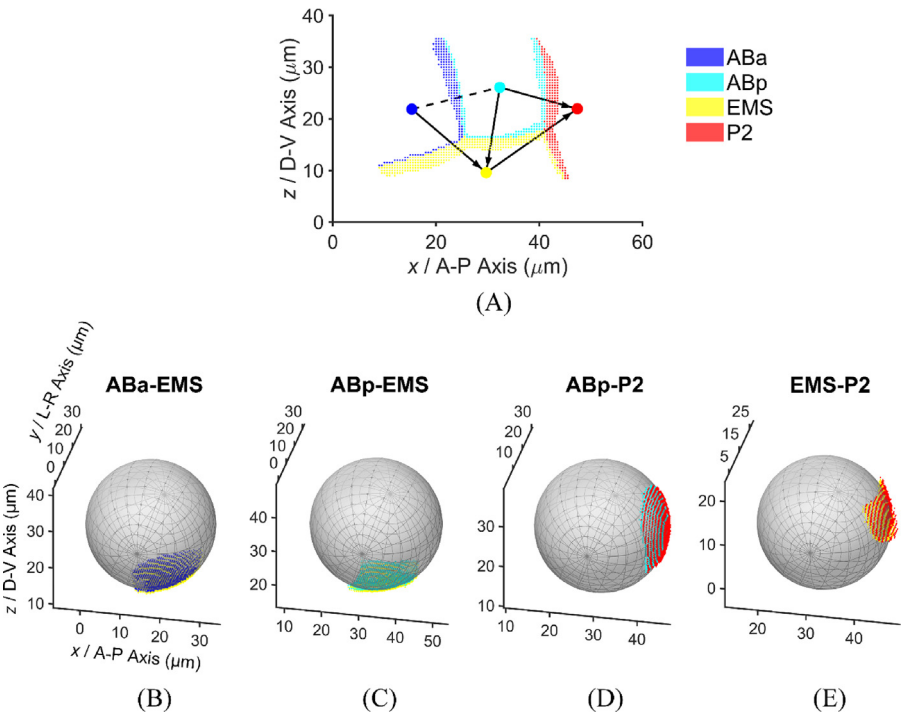

Fig. 8. Cell–cell interface curvation observed in experiment. (A) Cell–cell interface and its orientation (indicated by an arrow orienting from the inside of the fitted sphere) obtained from spherical surface fitting. The dashed line means that the ABa-ABp interface is near a plane and cannot be fitted with a sphere faithfully. (B, C, D, E) Spherical surface fitting of the ABa-EMS, ABp-EMS, ABp-P2, and EMS-P2 interfaces obtained from microscopic imaging and automatic segmentation. Each interface is shown with two layers of adjacent pixels that belong to the two neighbor cells respectively. A sphere fitted to the curved interface is shown in gray and has a radius equal to the fitted curvature radius. For the two neighbor cells forming an interface and a fitted sphere, the cell with pixels closer to the sphere protrudes toward the other one and therefore is stiffer, then the cell stiffness obeys ABa > EMS in (B), ABp > EMS in (C), ABp > P2 in (D), and EMS > P2 in (E).

irregularity (also called the dimensionless surface-to-volume ratio) as below:

$$\alpha_i = \frac{A_i^{\frac{1}{2}}}{V_i^{\frac{1}{3}}} \tag{15}$$

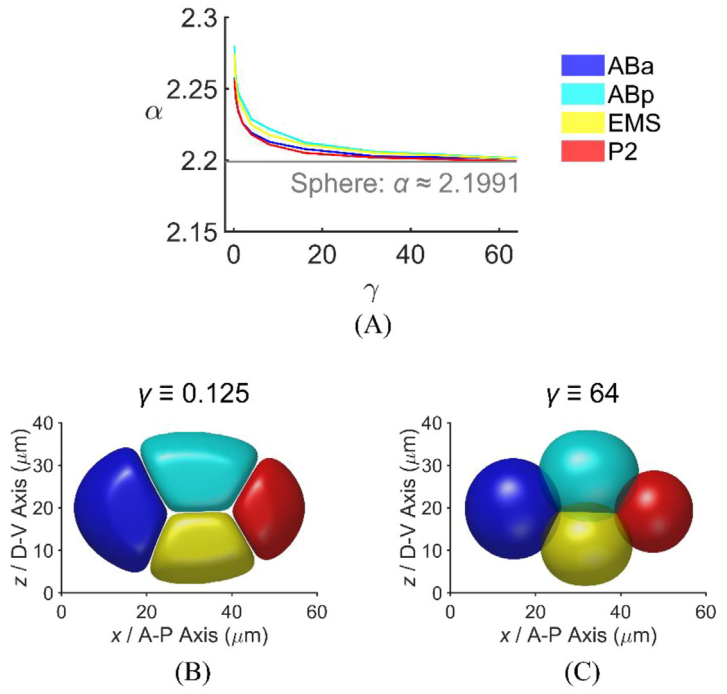

Fig. 9. The scanning of homogeneous cell stiffness at 4-cell stage in the phase-field model. (A) Cell shape irregularity α over cell stiffness γ. (B) The embryonic morphology with $\gamma \equiv 0.125$. (C) The embryonic morphology with $\gamma \equiv 64$.

which decreases over the face number of an object and has the smallest value as $2^{\frac{1}{3}} \cdot 3^{\frac{1}{3}} \cdot \pi^{\frac{1}{6}} \approx 2.199$ when it is a sphere. Using this factor, the cell shape irregularity in *C. elegans* embryogenesis has been reported to be lineage- and fate-dependent and associated with cell motility [11]. Here, we set $\sigma \equiv 0, M = 160, \delta t = 0.01$, and uniformly vary the cell stiffness γ at 4-cell stage in the phase-field model. As expected, the cell irregularity monotonically decreases over the cell stiffness and approaches the theoretical minimum (Fig. 9(A)). It is worth noting that the cell shape irregularity is distinguished even though the cell stiffness is assigned with the same value: the ABa and P2 have smaller α values while the ones of ABp and EMS are larger. The difference is caused by their positions, where ABa and P2 are located in the anterior and posterior poles of the embryo respectively, and each of them has only two cell–cell contact interfaces; however, ABp and EMS at the dorsal and ventral poles have three. The difference originates from the asymmetric eggshell shape and prismatic multicellular configuration, warning us that the environment geometry and cell position significantly affect the cell shape irregularity, so this morphological information might be insufficient for the cell-resolved inference of cell stiffness.

4.4. Convergence between the phase-field model and the coarse-grained model

In the previous section, we show that enhancing the cell stiffness leads the cell shape to a sphere in the phase-field model, and this morphological effect is attributed to the diffusive cell boundary (Eq. (6)). When $\gamma \gg g, \gamma \gg g_e, \gamma \gg \sigma$, the effect of repulsion and attraction on cell shape becomes very small and the surface tension becomes dominant. Thus, the cell shape turns to be spherical with increasing γ at equilibrium (Fig. 9(A)). Moreover, the cell–cell contact interface becomes a regional overlap between cells due to strong surface tension and conserved cell volume (Fig. 9(B) and (C)). In this limit condition, the morphological effect on the intercellular force is eliminated; in other words, the cell shape depicted by the phase field ϕ_i degrades to a single point with its spatial coordinates corresponding to the center of the phase field and a radius R_i, which is equivalent to the coarse-grained model (Figs. 5(B) and 9(C)). Consequently, the intercellular force is isotropic and can be treated as a function depending on the distance between two cells and their radii.

We then investigate the similarity of force–distance profiles between the phase-field model and coarse-grained model in the case of $\gamma \gg g, \gamma \gg g_e, \gamma \gg \sigma$. To this end, we perform simulations of two cells with $\gamma = 64, M = 160, \delta t = 0.01$, and $R = 10$ μm to get their spherical shapes at equilibrium. The force–distance profiles are obtained by introducing translational displacements between the two cells' phase fields, ϕ_i and ϕ_j, and the force exerted on cell i from cell j is calculated by:

$$F_{i,j} = \int_{\Omega} (\boldsymbol{F}_{\text{repulsion}} + \boldsymbol{F}_{\text{adhesion}}) \cdot \nabla \phi_i \mathrm{d}\boldsymbol{r}. \tag{16}$$

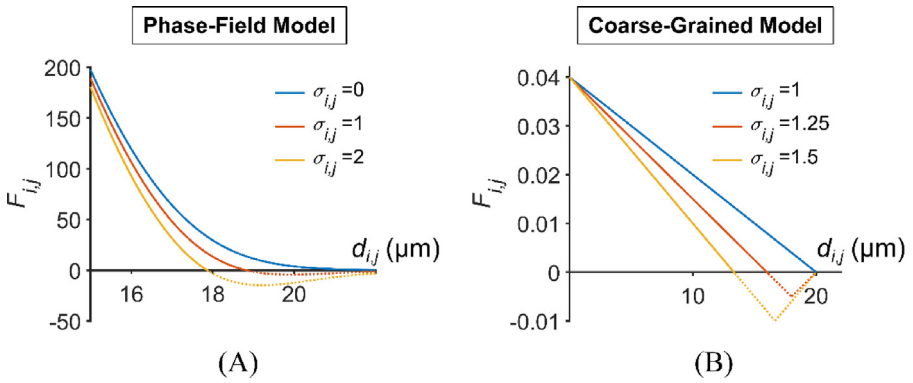

Fig. 10. The force between two cells with radii of 10 μm. (A) Results of the phase-field model with $\gamma = 64$. (B) Results of the coarse-grained model with $\gamma' = 0.04$.

The force–distance profiles show a repulsion–attraction transition depending on distance, which is consistent with the one in the coarse-grained model (Fig. 10 (A) and (B)) [20,34,50]. In both models, the balance distance where $F_{i,j} = 0$ changes in response to different strengths of cell adhesion σ, so the dynamics in the phase-field model converge to the ones in the coarse-grained model. Besides, the spring constant γ' that describes the cell stiffness and cell–cell repulsion in the coarse-grained model is now equivalent to the g in the phase-field model. The convergence between the two models indicates that the precise description of cell morphologies is the key to characterizing cell stiffness.

5. Limit of the phase-field model for reconstructing *in vivo* cell morphologies

5.1. Refinement of the mechanical parameters under known biological knowledge

So far, a total of five mechanical parameters at 4-cell stage (i.e., σ_S, σ_W, $\gamma_{ABa/ABp}$, γ_{EMS}, and γ_{P2}) are indicated by experimental evidence, which can be completely inferred by comparing *in vivo* and *in silico* cell morphologies using the phase-field model (Figs. 3, 4 (A) and (B), 6 (A) and (B)). Here, we devise an iteration pipeline to refine the value assignments $C = \{\sigma_S, \sigma_W, \gamma_{ABa/ABp}, \gamma_{EMS}, \gamma_{P2}\}$. The iteration is initialized with the final results in Fig. 6 (B), namely, $\sigma_S = 1.5, \sigma_W = 0.4, \gamma_{ABa/ABp} = 1.6, \gamma_{EMS} = 0.25, \gamma_{P2} = 0.15$, and the mean variation of cell shapes ($\overline{\eta}_{shape}$) is selected as the optimization target. For every round of iteration, each parameter is multiplied by 0.8, 0.9, 1.0, 1.1, and 1.2 so that the sub-region around it would be searched; consequently, $5^5 = 3125$ groups of simulations are conducted; the parameter combination with the minimal $\overline{\eta}_{shape}$ will be treated as the center of the scanning region in the next round of iteration. After five rounds of iteration, we reach the optimal parameter combination: $\sigma_S = 1.8, \sigma_W = 0, \gamma_{ABa/ABp} = 1.92, \gamma_{EMS} = 0.125, \gamma_{P2} = 0.09$.

5.2. Reconstruction of severe cell deformation and exploration of new biological mechanism

Under the constraint of cell shapes, the optimization of five mechanical parameters ends in $\overline{\eta}_{shape} = 0.161$ (Fig. 11 (A)). Next, we attempt to reconstruct the cell morphologies more precisely. First, in addition to the cell shape, we notice that the ABa-ABp and EMS-P2 contacts have the most deviated simulated areas compared to the experimental values ($\eta_{ABa,ABp} = 0.327, \eta_{EMS,P2} = 0.702$), so we introduce an assumption that the adhesion between ABa and ABp cells is even stronger, to separate it from the other contacts. Therefore, the adhesion setting is ternary: $\sigma_{ABa,ABp} = \sigma_S > \sigma_{ABa,EMS} = \sigma_{ABp,EMS} = \sigma_{ABp,P2} = \sigma_M > \sigma_{EMS,P2} = \sigma_W$. We adopt the value of 1.8 for σ_M and scan σ_S and σ_W again, achieving the global minimum where $\sigma_S = 5.6, \sigma_W = 0.2, \overline{\eta}_{contact} = 0.109$ and the variation of each cell–cell contact area is within 0.180 (Fig. 11 (B) and (C)). Second, regarding the cell shape, the EMS cell has the largest variation ($\eta_{EMS} = 0.222$); compared to the simulated structure, the real shape of EMS is much flatter (Figs. 2(D) and 11 (D)). To regenerate this phenotype, we set the $M = 40$ for stronger volume constriction, $\gamma_{ABa/ABp} = 10$ for higher cell stiffness, and $\sigma_{ABa,ABp} = 10$ for higher cell adhesion; then, decreasing the parameter σ_M can results in the flattened shape of EMS where η_{EMS} is lowered to 0.193 (Fig. 11(E)). Both improvements above are based on the addition of the ternary setting for cell adhesion. Interestingly, previous experimental research in *C. elegans* embryonic development proposed that the cortical tension could improve the enrichment of E-cadherin [29], while another experiment found that injection of actin inhibitor in a cell can eliminate its adhesion [51]. Provided that, we speculate that the heterogeneous cell stiffness at 4-cell stage may contribute to a more uneven adhesion distribution in cell–cell contacts, which molds the cell morphologies as seen *in vivo* and merits further verification.

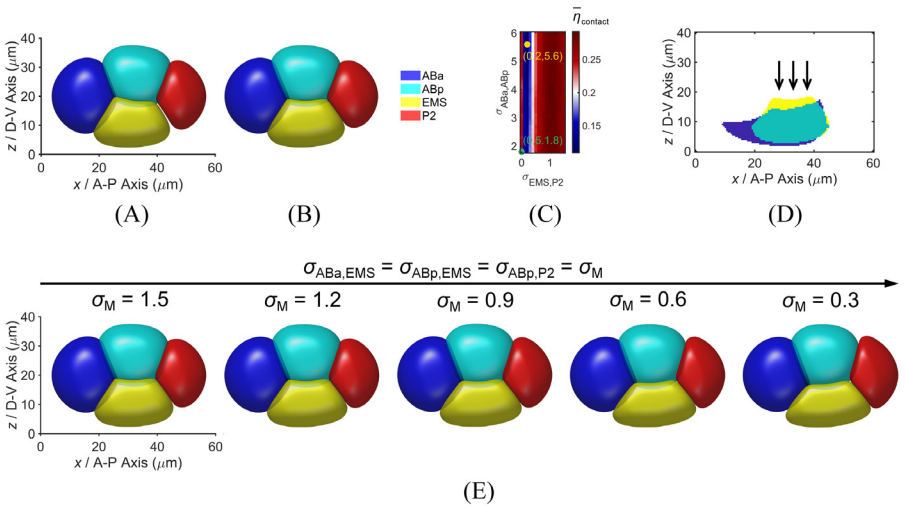

Fig. 11. Addition of ternary adhesion settings and shape reconstruction of EMS cell. The embryonic morphologies with binary and ternary adhesion settings are shown in (A) and (B). (C) The parameter scanning of $\sigma_{ABa,ABp}$ and $\sigma_{EMS,P2}$ and the outputted mean variations of cell–cell contact areas ($\overline{\eta}_{contact}$) are illustrated by heatmap, with the yellow and green points labeling the optimal and original values respectively. (D) The shape difference of EMS cell between simulation in (B) and experiment; the overlap is painted cyan, while the missing and extra regions in simulation are painted blue and yellow respectively. (E) Embryonic morphologies with different value assignments of σ_M.

6. Conclusions and perspectives

Cellular morphology and mechanics play a pivotal role in all kinds of biological phenomena such as embryogenesis and morphogenesis. Due to the complex interactions and the difficulty of quantitative measurement in experiments, it is significantly challenging for mathematical modeling to obtain accurate cellular morphological and mechanical information. Thanks to the advanced technology for monitoring *C. elegans* embryonic development, the researchers acquired the ground truth of cell positions, cell morphologies, and force distributions to test the mechanical models. In this paper, we comprehensively investigated two popular models, i.e. the phase-field model and the coarse-grained model, and compared their performance in recapitulating cellular morphological and mechanical properties in reality at single-cell resolution. On the one hand, by fitting the cell–cell contact areas *in vivo* and *in silico*, the heterogeneous cell adhesion distribution can be derived by both models. On the other hand, the phase-field model succeeds in inferring the heterogeneous cell stiffness but the coarse-grained model fails.

The inference method above is computationally efficient, as a phase-field simulation (in GPU) or a coarse-grained simulation (in CPU) for 2- and 4-cell stages costs no longer than 2 min, so it could be applied to the later developmental stages of *C. elegans* embryogenesis as well as other multicellular systems (Table S4) [9–11]. Further, more morphological features (e.g., the contact angle among cell–cell interfaces) can be explored as well, and a weighted error function incorporating multiple morphological features may help infer the mechanical properties and reconstruct the experimental morphologies more accurately [21,52]. It should be pointed out that the spatial resolution of microscopy and segmentation has to be high enough for depicting the morphological features of a cell, otherwise the information on mechanical properties would be lost and not inferable; the same requirement also exists in the phase-field simulation, where the spatial resolution of the grid has to be high enough for maintaining computational accuracy and depicting cellular morphology [38]. In particular, for the lower heterogeneity of cell stiffness, the spatial resolution needs to be higher so that the slight curvature in the interface between two cells can be captured both *in vivo* and *in silico*; likewise, higher spatial resolution is needed for distinguishing the smaller difference in cell adhesion and cell–cell contact area.

Although the phase-field model is capable of characterizing both the cell adhesion and cell stiffness in reality by minimizing the difference between *in vivo* and *in silico* cell morphologies, the mean variation of cell shapes ($\overline{\eta}_{shape}$) keeps larger than 0.150 throughout all simulations. Four possible reasons account for this discrepancy: 1. The shape of *C. elegans* eggshell we used resembles an ellipsoid, but a recent study reported that the real one is more like a capsule, where the curvatures of the anterior and posterior poles are much smaller. Notably, the capsule-like boundary was found to be essential for reproducing the cell-arrangement patterns seen *in vivo* [37]. 2. The actual distribution of cell adhesion and cell stiffness may be more complicated than our binary or ternary settings. Instead, the adhesion of each cell–cell contact and the stiffness of each cell are probably different to some extent. 3. More biological processes may need to be included for simulating the real situation, such as cytoskeleton dynamics, local constriction, cell polarization, and random noise [53–56]. 4. The current mathematical formula does not fit reality perfectly. On the one hand, regarding cell adhesion, the area of ABa-ABp contact in simulation is always smaller than the value measured experimentally; it is distinguishable that the periphery of their interface almost reaches the eggshell in a live embryo, while the simulated one is dented. In

the current formulation of cell adhesion (Eq. (5)), the force intensity in the interface center is relatively stronger than the one in the periphery, which causes numerical instability, limits the value assignment of σ, and perhaps violates the real situation. On the other hand, regarding cell stiffness, some relevant mechanical factors beyond cell surface tension (e.g., the viscoelasticity and bending resistance of the cell cortex) might be non-ignorable for reconstructing cell shape more accurately and need to be incorporated in the future [57,58]. Importantly, the morphological variation can reveal the model performance and help answer which part of forces is described inappropriately and what kind of new mechanisms need to be added.

In addition to the phase-field model, we found that the coarse-grained model, which simplifies a cell into a single point, can also infer the heterogeneous cell adhesion distribution by fitting the cell–cell contact area measured experimentally. It is attributed to the simple rule that the contact area is positively correlated to cell adhesion and negatively correlated to intercellular distance. Thus, we expect that the models whose complexity lies between the coarse-grained and phase-field ones (e.g., the vertex model and multi-particle model) are also capable of describing cell adhesion and cell–cell contact area as well [30,31,59,60]. On the other hand, although some models regard cell stiffness as just an antagonistic against cell adhesion (with an equivalent effect in leading to a longer distance or a smaller contact area between neighbor cells) [21], we found that the cell–cell interface curvature is substantially coupled with heterogeneous cell stiffness and should be considered seriously when cell shape is a focused problem. Thus, it is a considerable improvement direction for the coarse-grained model and others to generate the curved cell–cell interface that fits the real one [61,62]. Concerning the high computational cost of the phase-field model, it is a useful strategy to take advantage of the coarse-grained model to roughly evaluate the cell–cell interaction first when the cell number is in dozens to hundreds; then the phase-field model could be employed to refine the mechanical parameters and generate the cell shapes. It is also meaningful to use the *in vivo* cell morphology as ground truth and develop new agent-based physical models, whose complexity is between the coarse-grained and phase-field ones, for instance, the vertex model and multi-particle model [30,31,63,64].

CRediT authorship contribution statement

Guoye Guan: Conceptualization, Data curation, Formal analysis, Investigation, Software, Validation, Visualization, Writing – original draft. **Xiangyu Kuang:** Conceptualization, Data curation, Formal analysis, Investigation, Software, Validation, Visualization, Writing – original draft. **Chao Tang:** Conceptualization, Funding acquisition, Investigation, Project administration, Resources, Supervision, Validation, Writing – review & editing. **Lei Zhang:** Conceptualization, Funding acquisition, Investigation, Project administration, Resources, Supervision, Validation, Writing – review & editing.

Declaration of competing interest

The authors declare the following financial interests/personal relationships which may be considered as potential competing interests: Lei Zhang reports financial support was provided by Peking University.

Data availability

The data and code for producing the analyses described can be accessed in https://doi.org/10.6084/m9.figshare.21070141.

Acknowledgments

This work was supported by the National Key Research and Development Program of China (Grant No. 2021YFF1200500) and the National Natural Science Foundation of China (Grant Nos. 12225102, 12050002, 12226316, 12090053, 32088101).

Appendix A. Details of the eggshell setting

The eggshell is idealized as an ellipsoid with the semi-axes $L_{x/\mathrm{A-P}} = 27.7846$ μm and $L_{z/\mathrm{D-V}} = 18.3778$ μm, provided by the original literature of the experimental dataset, which searched the minimal cylindroid that encloses the whole embryos [11]; the values of $L_{x/\mathrm{A-P}}$ and $L_{z/\mathrm{D-V}}$ have been averaged over 17 embryo samples. Considering the artificial compression during confocal microscopy imaging, we set the other semi-axis $L_{y/\mathrm{L-R}} = 14.7022$ μm, with 20% less than $L_{z/\mathrm{D-V}}$, to mimic the amplified curvature of the embryo's periphery. Besides, the regions $|y| > w_{\max} = \frac{w_{\max,6-\mathrm{Cell}}+w_{\max,7-\mathrm{Cell}}+w_{\max,8-\mathrm{Cell}}}{3} = 10.1188$ μm are removed because of lateral compression, where $w_{\max,6-\mathrm{Cell}}$, $w_{\max,7-\mathrm{Cell}}$, and $w_{\max,8-\mathrm{Cell}}$ are the maximal distance of the cellular regions to the *xz* plane at 6-, 7-, and 8-cell stages, respectively. The eggshell shape described above is termed "Eggshell Shape 1" in this paper.

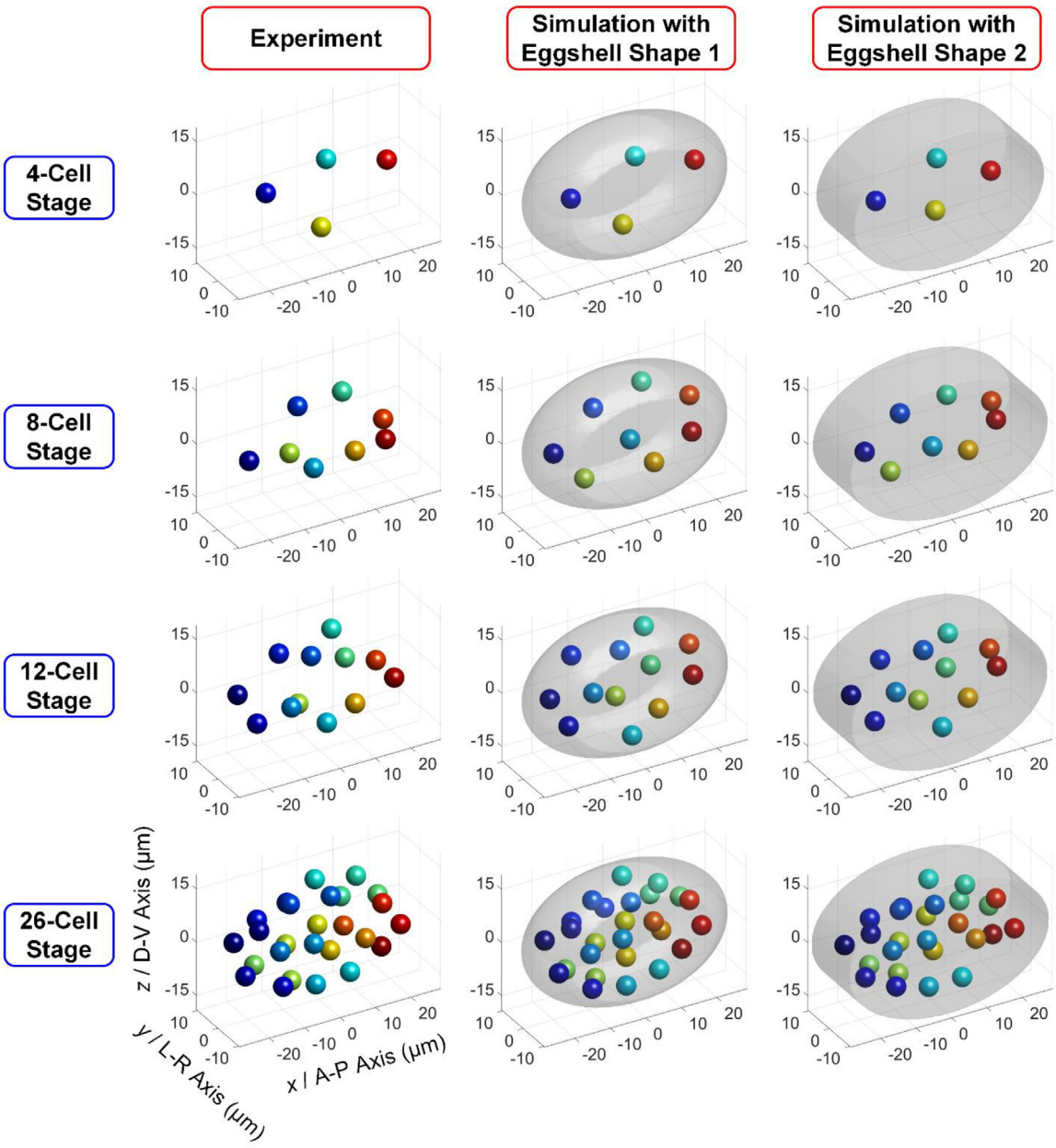

Fig. 12. Cell-arrangement patterns in the experiment and simulations with the coarse-grained model ($\gamma' = 0.04$, $\frac{1}{\sigma} = 0.85$) at 4-, 8-, 12-, and 26-cell stages. The experimental cell positions are averaged over 46 embryo samples from [11]. The simulated cell positions are illustrated with their final states when *in silico* time = 2000.

Appendix B. Details of the coarse-grained model

To adapt the latest *C. elegans* embryo data and the eggshell shape ("Eggshell Shape 1") used in this paper, we adopt and optimize the pipeline used before to fit the mechanical parameters in the coarse-grained model: cell adhesion σ and cell stiffness γ' [34]:

A. Preliminary Test for Restoring Force: All cells are initially placed at their experimental positions and the resultant force $\boldsymbol{f}$ imposed on each cell from its neighbors and eggshell is calculated. Then the cell position is imaginarily translated along the orientation of $\boldsymbol{f}$ with a distance of its equivalent radius. If the cell at the new position is subject to a resultant force $\boldsymbol{f}'$ that has a weight in the opposite orientation of $\boldsymbol{f}$, the $\boldsymbol{f}'$ is regarded to have an effect as a restoring force and avoid the severe deviation of cell position.

B. Movement Test for Cell Position: All cells are initially placed at their experimental positions and allowed to move for an *in silico* time = 2000 with a time step of 0.1. The system is requested to approach mechanical equilibrium quickly, reaching a final root-mean-square velocity of less than 0.05. Apart, the distance between the final cell positions and the experimental ones must be shorter than the equivalent cell radius, ensuring that the stereotypic cell-arrangement patterns are recapitulated.

The two steps above are executed for the embryonic structures at the last moment of 4-, 8-, 12-, and 26-cell stages, when all the cells have separate membranes [11]. The first step filters the parameter roughly while the second step further validates the suitability of the parameter assignments. Both steps are first carried out on the elliptical cylinder fitted with imaging data before (termed as "Eggshell Shape 2") [11]. With respect to the refined parameters, they are required to pass the movement test with the eggshell in Appendix A ("Eggshell Shape 1") as well. We set $\gamma' = 0.02 : 0.02 : 1.00$ (no stiffer than the eggshell, i.e., $\gamma_e = 1$) and $\frac{1}{\sigma} = 0.70 : 0.05 : 1.00$ (the balance distance no longer than the sum of cell radii, i.e., $\frac{1}{\sigma_{i,j}}\left(R_i + R_j\right) < \left(R_i + R_j\right)$). Eventually, there are three sets of parameters satisfying all the criteria: 1. $\gamma' = 0.02$, $\frac{1}{\sigma} = 0.80, 0.85, 0.90$; 2. $\gamma' = 0.04$, $\frac{1}{\sigma} = 0.80, 0.85$; 3. $\gamma' = 0.06$, $\frac{1}{\sigma} = 0.85$. Hence, we choose the central values $\gamma' = 0.04$, $\frac{1}{\sigma} = 0.85$, whose corresponding simulation results are illustrated in Fig. 12.

Appendix C. Supplementary data

Supplementary material related to this article can be found online at https://doi.org/10.1016/j.cnsns.2022.106966.

References

[1] Fujita M, Onami S. Cell-to-cell heterogeneity in cortical tension specifies curvature of contact surfaces in *Caenorhabditis elegans* embryos. PLoS One 2012;7:e30224.
[2] Chan Y-HM. Growth: A model for establishing cell size and shape. Curr Biol 2016;26:R767–9.
[3] Rens EG, Merks RMH. Cell shape and durotaxis explained from cell-extracellular matrix forces and focal adhesion dynamics. iScience 2020;23:101488.
[4] Kuang X, Guan G, Wong M-K, Chan L-Y, Zhao Z, Tang C, et al. Computable early *Caenorhabditis elegans* embryo with a phase field model. PLoS Comput Biol 2022;18:e1009755.
[5] Luxenburg C, Zaidel-Bar R. From cell shape to cell fate via the cytoskeleton - Insights from the epidermis. Exp Cell Res 2019;378:232–7.
[6] Frey F, Idema T. More than just a barrier: Using physical models to couple membrane shape to cell function. Soft Matter 2021;17:3533–49.
[7] Cross SE, Jin Y-S, Rao J, Gimzewski JK. Nanomechanical analysis of cells from cancer patients. Nat Nanotechnol 2007;2:780–3.
[8] Luo Q, Kuang D, Zhang B, Song G. Cell stiffness determined by atomic force microscopy and its correlation with cell motility. Biochim Biophys Acta Gen Subj 2016;1860:1953–60.
[9] Stegmaier J, Amat F, Lemon WC, McDole K, Wan Y, Teodoro G, et al. Real-time three-dimensional cell segmentation in large-scale microscopy data of developing embryos. Dev Cell 2016;36:225–40.
[10] Leggio B, Laussu J, Carlier A, Godin C, Lemaire P, Faure E. MorphoNet: An interactive online morphological browser to explore complex multi-scale data. Nature Commun 2019;10:2812.
[11] Cao J, Guan G, Ho VWS, Wong M-K, Chan L-Y, Tang C, et al. Establishment of a morphological atlas of the *Caenorhabditis elegans* embryo using deep-learning-based 4D segmentation. Nature Commun 2020;11:6254.
[12] Sawyer JM, Harrell JR, Shemer G, Sullivan-Brown J, Roh-Johnson M, Goldstein B. Apical constriction: A cell shape change that can drive morphogenesis. Dev Biol 2010;341:5–19.
[13] Heisenberg C-P, Bellaïche Y. Forces in tissue morphogenesis and patterning. Cell 2013;153:948–62.
[14] Hannezo E, Heisenberg C-P. Rigidity transitions in development and disease. Trends Cell Biol 2022;32:433–44.
[15] Simon A, Durrieu M-C. Strategies and results of atomic force microscopy in the study of cellular adhesion. Micron 2006;37:1–13.
[16] Thomas G, Burnham NA, Camesano TA, Wen Q. Measuring the mechanical properties of living cells using atomic force microscopy. J Vis Exp 2013;76:e50497.
[17] Kilian KA, Bugarija B, Lahn BT, Mrksich M. Geometric cues for directing the differentiation of mesenchymal stem cells. Proc Natl Acad Sci USA 2010;107:4872–7.
[18] Jelier R, Kruger A, Swoger J, Zimmermann T, Lehner B. Compensatory cell movements confer robustness to mechanical deformation during embryonic development. Cell Syst 2016;3:160–71.
[19] Brodl GW, Veldhuis JH, Kim S, Perrone M, Mashburn D, Hutson MS. CellFIT: A cellular force-inference toolkit using curvilinear cell boundaries. PLoS One 2014;9:e99116.
[20] Yamamoto K, Kimura A. An asymmetric attraction model for the diversity and robustness of cell arrangement in nematodes. Development 2017;144:4437–49.
[21] Petridou NI, Corominas-Murtra B, Heisenberg C-P, Hannezo E. Rigidity percolation uncovers a structural basis for embryonic tissue phase transitions. Cell 2021;184:1914–28.
[22] Jilkine A, Edelstein-Keshet L. A comparison of mathematical models for polarization of single eukaryotic cells in response to guided cues. PLoS Comput Biol 2011;7:e1001121.
[23] Holmes WR, Edelstein-Keshet L. A comparison of computational models for eukaryotic cell shape and motility. PLoS Comput Biol 2012;8:e1002793.
[24] Osborne JM, Fletcher AG, Pitt-Francis JM, Maini PK, Gavaghan DJ. Comparing individual-based approaches to modelling the self-organization of multicellular tissues. PLoS Comput Biol 2017;13:e1005387.
[25] Schnabel R, Hutter H, Moerman D, Schnabel H. Assessing normal embryogenesis in *Caenorhabditis elegans* using a 4D microscope: Variability of development and regional specification. Dev Biol 1997;184:234–65.
[26] Murray JI, Bao Z, Boyle TJ, Waterston RH. The lineaging of fluorescently-labeled *Caenorhabditis elegans* embryos with StarryNite and AceTree. Nat Protoc 2006;1:1468–76.
[27] Sulston JE, Schierenberg E, White JG, Thomson JN. The embryonic cell lineage of the nematode *Caenorhabditis elegans*. Dev Biol 1983;100:64–119.
[28] Guan G, Wong M-K, Ho VWS, An X, Chan L-Y, Tian B, et al. System-level quantification and phenotyping of early embryonic morphogenesis of *Caenorhabditis elegans*. 2019, 776062, bioRxiv.

[29] Marston DJ, Higgins CD, Peters KA, Cupp TD, Dickinson DJ, Pani AM, et al. MRCK-1 drives apical constriction in *C. elegans* by linking developmental patterning to force generation. Curr Biol 2016;26:2079–89.
[30] Kajita A, Yamamura M, Kohara Y. Physical modeling of the cellular arrangement in *C. elegans* early embryo: Effect of rounding and stiffening of the cells. Genome Inform 2002;13:224–32.
[31] Kajita A, Yamamura M, Kohara Y. Computer simulation of the cellular arrangement using physical model in early cleavage of the nematode *Caenorhabditis elegans*. Bioinformatics 2003;19:704–16.
[32] Fickentscher R, Struntz P, Weiss M. Mechanical cues in the early embryogenesis of *Caenorhabditis elegans*. Biophys J 2013;105:1805–11.
[33] Fickentscher R, Struntz P, Weiss M. Setting the clock for fail-safe early embryogenesis. Phys Rev Lett 2016;117:188101.
[34] Guan G, Tang L-H, Tang C. Reconstructing the multicellular structure of a developing metazoan embryo with repulsion-attraction model and cell–cell connection atlas *in vivo*. J Phys: Conf Ser 2020;1592:012020.
[35] Miao J, Guan G, Tang C. Spontaneous mechanical and energetic state transitions during *Caenorhabditis elegans* gastrulation. 2022, arXiv:2105.05795v2.
[36] Jiang J, Garikipati K, Rudraraju S. A diffuse interface framework for modeling the evolution of multi-cell aggregates as a soft packing problem driven by the growth and division of cells. Bull Math Biol 2019;81:3282–300.
[37] Seirin-Lee S, Yamamoto K, Kimura A. The extra-embryonic space and the local contour are crucial geometric constraints regulating cell arrangement. Development 2022;149:dev200401.
[38] Kuang X, Guan G, Tang C, Zhang L. MorphoSim: An efficient and scalable phase-field framework for accurately simulating multicellular morphologies. 2022, arXiv:2206.04903.
[39] Tian B, Guan G, Tang L-H, Tang C. Why and how the nematode's early embryogenesis can be precise and robust: A mechanical perspective. Phys Biol 2020;17:026001.
[40] Darling EM, Zauscher S, Block JA, Guilak F. A thin-layer model for viscoelastic, stress-relaxation testing of cells using atomic force microscopy: Do cell properties reflect metastatic potential? Biophys J 2007;92:1784–91.
[41] Friedl P, Wolf K, Lammerding J. Nuclear mechanics during cell migration. Curr Opin Cell Biol 2011;23:55–64.
[42] Shao D, Rappel WJ, Levine H. Computational model for cell morphodynamics. Phys Rev Lett 2010;105:108104.
[43] Hench J, Henriksson J, Lüppert M, Bürglin TR. Spatio-temporal reference model of *Caenorhabditis elegans* embryogenesis with cell contact maps. Dev Biol 2009;333:1–13.
[44] Wang Z, Wang D, Li H, Bao Z. Cell neighbor determination in the metazoan embryo system. In: Proceedings of the 8th ACM international conference on bioinformatics, computational biology, and health informatics. 2017, p. 305–12.
[45] Chen L, Ho VWS, Wong M-K, Huang X, Chan L-Y, Ng HCK, et al. Establishment of signaling interactions with cellular resolution for every cell cycle of embryogenesis. Genetics 2018;209:37–49.
[46] Wang Z, Xu Y, Wang D, Yang J, Bao Z. Hierarchical deep reinforcement learning reveals a modular mechanism of cell movement. Nat Mach Intell 2022;4:73–83.
[47] Brauchle M, Baumer K, Gönczy P. Differential activation of the DNA replication checkpoint contributes to asynchrony of cell division in *C. elegans* embryos. Curr Biol 2003;13:819–27.
[48] Schumacher B, Alpi A, Garter A. Cell cycle: Check for asynchrony. Curr Biol 2003;13. R560-2.
[49] Fujii Y, Koizumi WC, Imai T, Yokobori M, Matsuo T, Oka K, et al. Spatiotemporal dynamics of single cell stiffness in the early developing ascidian chordate embryo. Commun Biol 2021;4:341.
[50] Koyama H, Okumura H, Ito AM, Otani T, Nakamura K, Kato K, et al. Effective mechanical potential of cell–cell interaction explains basic structures of three-dimensional morphogenesis. 2021, 812198, bioRxiv.
[51] Kikuchia Y, Kimura A. Microinjection into the *Caenorhabditis elegans* embryo using an uncoated glass needle enables cell lineage visualization and reveals cell-non-autonomous adhesion control. 2018, 406991, bioRxiv.
[52] Boyer F, Lapuerta C. Study of a three component Cahn-Hilliard flow model. ESAIM Math. Model. Numer. Anal. 2006;40:653–87.
[53] Camley BA, Zhao Y, Li B, Levine H, Rappel W-J. Periodic migration in a physical model of cells on micropatterns. Phys Rev Lett 2013;111:158102.
[54] An Y, Xue G, Zhou X, Yu W, Ishibashi T, Zhang L, et al. Apical constriction is driven by a pulsatile apical myosin network in delaminating *Drosophila* neuroblasts. Development 2017;144:2153–64.
[55] Wang W, Tao K, Wang J, Yang G, Ouyang Q, Wang Y, et al. Exploring the inhibition effect of membrane tension on cell polarization. PLoS Comput Biol 2017;13:e1005354.
[56] Tao K, Wang J, Kuang X, Wang W, Liu F, Zhang L. Tuning cell motility via cell tension with a mechanochemical cell migration model. Biophys J 2020;118:2894–904.
[57] Tanaka H, Araki T. Viscoelastic phase separation in soft matter: Numerical-simulation study on its physical mechanism. Chem Eng Sci 2006;61:2108–41.
[58] Wang X, Du Q. Modelling and simulations of multi-component lipid membranes and open membranes via diffuse interface approaches. J Math Biol 2008;56:347–71.
[59] Nagai T, Ohta S, Kawasaki K, Okuzono T. Computer simulation of cellular pattern growth in two and three dimensions. Phase Transit 1990;28:177–211.
[60] Fuchizaki K, Kusaba T, Kawasaki K. Computer modelling of three-dimensional cellular pattern growth. Phil Mag B 1995;71:333–57.
[61] Ishimoto Y, Morishita Y. Bubbly vertex dynamics: A dynamical and geometrical model for epithelial tissues with curved cell shapes. Phys Rev E 2014;90:052711.
[62] Kaliman S, Jayachandran C, Rehfeldt F, Smith A-S. Limits of applicability of the voronoi tessellation determined by centers of cell nuclei to epithelium morphology. Front Physiol 2016;7:551.
[63] Sussman DM, Schwarz JM, Marchetti MC, Manning ML. Soft yet sharp interfaces in a vertex model of confluent tissue. Phys Rev Lett 2018;120:058001.
[64] Luciano M, Xue S-L, Vos WHDe, Redondo-Morata L, Surin M, Lafont F, et al. Cell monolayers sense curvature by exploiting active mechanics and nuclear mechanoadaptation. Nat Phys 2021;17:1382–90.